Nitrogen-doped Multi-walled Carbon Nanotubes-MnCo$_2$O$_4$ microsphere as electrocatalyst for efficient oxygen reduction reaction

S. Yuvaraj [a], A. Vignesh [b], S. Shanmugam [b,**], R. Kalai Selvan [a,*]

[a] Solid State Ionics and Energy Devices Laboratory, Department of Physics, Bharathiar University, Coimbatore, 641 046, Tamil Nadu, India

[b] Department of Energy Systems Engineering, Daegu Gyeongbuk Institute of Science and Technology (DGIST), Daegu, 711-873, South Korea

ARTICLE INFO

ABSTRACT

Nitrogen-doped Multi-walled Carbon Nanotubes (N-doped MWCNT)/MnCo$_2$O$_4$ hybrid is synthesized by a facile hydrothermal method. The X-ray diffraction studies revealed the single phase formation of cubic spinel structured MnCo$_2$O$_4$ and their composites. The presence of D and G band of MWCNT is identified through Raman spectral analysis. The elemental oxidation state and nitrogen content is obtained using X-ray photoelectron spectroscopy, which elucidates that Co and Mn exists in multivalence state and the nitrogen functional groups are in pyrolytic and pyridinic-type. FE-SEM shows the microsphere formation of MnCo$_2$O$_4$ and size exhibits in the range of 6—9 μm. The N-doped MWCNT/MnCo$_2$O$_4$ hybrid catalyst exhibits an improved oxygen reduction electrocatalytic activity in an aqueous alkaline medium when compared with pristine MnCo$_2$O$_4$.

Introduction

The oxygen reduction reaction (ORR) is the state of art reaction for the development of advanced clean energy storage devices like metal-air batteries, fuel cells and electrochemical treatment of waste water contamination [1—3]. It is well known that ORR is sluggish and complex in nature and this reaction takes place in two parallel ways. Transfer of four electrons with the formation of H$_2$O is one way and transfer of two electrons with the generation of hydrogen peroxide is the other way [4]. However, the sluggish kinetics of ORR is one of the major challenges. Normally, Pt and its alloys are considered as good candidates for ORR activity due to its low over potential and high current density [5]. But, its high cost and low abundance as well as sluggish kinetics prohibit the use of commercial application [6,7]. So it is opened up a new avenue to develop a Pt-free electrocatalyst to enhance the electrocatalytic activities for the multifunctional electrochemical applications [8].

Recently, ORR activity of transition metal oxides including Co$_3$O$_4$, Mn$_3$O$_4$ and α-Fe$_2$O$_3$ were broadly investigated due to their high electrochemical activity, low cost, high abundance and the environmental friendliness [4,9,10]. Among these catalysts, Co and Mn based oxides showed an excellent performance, but their poor electronic conductivity affects the

reaction kinetics. Further, the researchers are mainly focused on manganese based spinel structured compounds like $Mn_xCo_{3-x}O_4$ [11], $Co_xMn_{3-x}O_4$ [12], $MnCo_2O_4$ [13,14] and $CaMn_2O_4$ [15]. The main advantageous properties of this type of spinel metal oxides are higher electronic conductivity due to its low activation energy and electron transfer between the neighbouring cations. Here, the multiple valence state of the cations facilitates higher ORR activity by providing donor-acceptor chemi-sorption sites for reversible adsorption of oxygen [16]. Prabu et al. have reported that the higher oxidation state of Ni and Co metal ions considerably increased the electrocatalytic activities of $NiCo_2O_4$ due to the presence of trivalent ions in the spinel structure [17]. Rios et al. has reported that the manganese catalyst, i.e., $Mn_xCo_{3-x}O_4$ mixed spinel provided ORR, but it restricted the oxygen evolution reaction (OER) activity [11]. On the other hand, Cheng et al. has prepared both cubic and tetragonal phase of $Co_xMn_{3-x}O_4$ and reported that both the phases favoured the ORR and OER activity, which depend upon the different binding energies of adsorbed oxygen on Co and Mn defect sites [12]. Wang et al. has reported that the catalytic activity of Co_2FeO_4 was increased while reducing the particle size from micro to nano-level, since the surface to volume ratio increased as well as this nano regime improved the reaction sites [18]. Further, the metal oxides anchored CNT acted as best catalyst support, since CNT has high electrical conductivity, structural flexibility, high mechanical strength and large surface area [19–22]. While dispersing metal oxides on the surface of CNT, it improved the electronic conductivity which in turn excellent electrocatalytic activities than the pristine compounds. Overall, it can be concluded that the electrocatalytic activities is attributed by different factors like crystal phases, oxidation state, morphology, surface area and electronic conductivity.

In this context, the present work concentrated on the electrocatalytic ORR activities of inverse spinel structured $MnCo_2O_4$, since both the Mn and Co metal cations are existing in mixed valence state [23]. Here, the $MnCo_2O_4$ microsphere is prepared by a facile hydrothermal method. Subsequently, the $MnCo_2O_4$ is supported on N-doped MWCNT to enhance the electrocatalytic activity through altering the electronic conductivity of pristine $MnCo_2O_4$. The prepared sample is analyzed by various characterization techniques like XRD, Raman, XPS and FE-SEM analysis. The electrocatalytic activities of prepared $MnCo_2O_4$ and N-doped $MWCNT-MnCo_2O_4$ are analyzed through the oxygen reduction reaction in alkaline medium.

Experimental details

The spinel structured $MnCo_2O_4$ was prepared using the starting precursor of $Co(CH_3COO)_2 \cdot 4H_2O$, $Mn(CH_3COO)_2 \cdot 4H_2O$, ascorbic acid and ammonia solution, which were purchased from Merck Pvt. Ltd, Mumbai. For the typical synthesis, the stoichiometric amount of $Co(CH_3COO)_2 \cdot 4H_2O$ (0.996 g) and $Mn(CH_3COO)_2 \cdot 4H_2O$ (0.49 g) was dissolved in 30 mL of water. Further, 0.704 g of ascorbic acid was dissolved in 10 mL of water and added into the above mixed solution. The pH of the solution was maintained at 12 by adding 1.8 mL of ammonia solution after that the solution was transferred into Teflon lined stainless steel container and kept at 200 °C for 24 h under

hydrothermal treatment. The hydrothermal set up was allowed to cool naturally and the obtained resulting powder was washed with distilled water and ethanol to remove the unwanted residues. Then the powder was dried at 80 °C for 12 h and calcinated at 500 and 800 °C for 3 h.

For the functionalization of MWCNT, 0.5 g of MWCNT was dispersed in 3:1 ratio of H_2SO_4 and HNO_3 solution and refluxed at 110 °C for 6 h after that the MWCNT was washed with distilled water until the pH was reached at 7 and then dried at 80 °C for 24 h. For the preparation of $MWNCNT-MnCo_2O_4$ hybrid, 0.1 g of functionalized MWCNT was mixed with the starting precursors of $MnCo_2O_4$ and kept at 200 °C for 24 h to obtain the composite of $MWCNT-MnCo_2O_4$. Subsequently, it was calcinated at 500 °C for 3 h under Ar atmosphere. Hereafter, the samples denoted as M1 (as prepared $MnCo_2O_4$ calcinated at 500 °C), M2 (as prepared N-doped $MWCNT/MnCo_2O_4$ calcinated at 500 °C) and M3 (as prepared $MnCo_2O_4$ calcinated at 800 °C).

X-ray diffraction analysis was carried out using D2 PHASER desktop diffractometer using Cu Kα radiation (λ = 1.541 Å). Raman analysis was performed on the samples through Horiba Jobin Yvon instrument with λ = 514 nm laser source in the frequency range of 100 cm^{-1} – 3000 cm^{-1}. The valence state of the elements was analyzed using AXIS ULTA-AXIS 165 X-ray Photoelectron Spectrometer (Kratos Analytical). The morphology of the sample was examined using FEI Quanta-250 Field Emission Scanning Electron Microscopy (FE-SEM). The ORR activity measurements was carried out using computer-controlled potentiostat (Bio-logic) instrument and all electro-chemical experiments were carried out at a scan rate of 10 mVs^{-1} and the experimental setup comprises of glassy carbon or rotating disk electrode, Pt wire and standard calomel electrode (SCE) used as working, counter and reference electrodes, respectively. All the potentials reported in this work were against reversible hydrogen electrode (RHE). The as synthesized M1, M2 and M3 catalysts were evaluated for electrochemical activity for oxygen reduction reaction (ORR) under alkaline condition of 0.1 M KOH electrolyte. The catalyst ink was prepared by dispersing 5 mg of catalyst in a solvent consists of 160 μl of iso propyl alcohol (IPA), 30 μL of deionized water and 10 μL of Nafion (5 wt %) were thoroughly ultrasonicated for 30 min in order to obtain a well dispersed catalyst ink. The catalyst ink was dropped on to the surface of a glassy carbon electrode and dried at room temperature. The electrocatalytic behaviour of N-doped $MWCNT/MnCo_2O_4$ was evaluated using a loading of 0.25 mg cm^{-2} on the glassy carbon electrode.

Results and discussion

To identify the phase purity of the $MnCo_2O_4$, the XRD analysis is carried out and are given in Fig. 1. Fig. 1(a) shows the XRD pattern of as-prepared $MnCo_2O_4$ and their diffraction peaks are indexed with the hexagonal phase of metal carbonates such as $CoCO_3$ and $MnCO_3$ that confirms through standard JCPDS file no. 78-0209 and 85-1109, respectively. During the synthesis process, ascorbic acid act as a reducing agent by oxidizing of C=C bond and it reduces the pH of the solution by generation of H^+ ions that leads to the formation of metal carbonates [24].
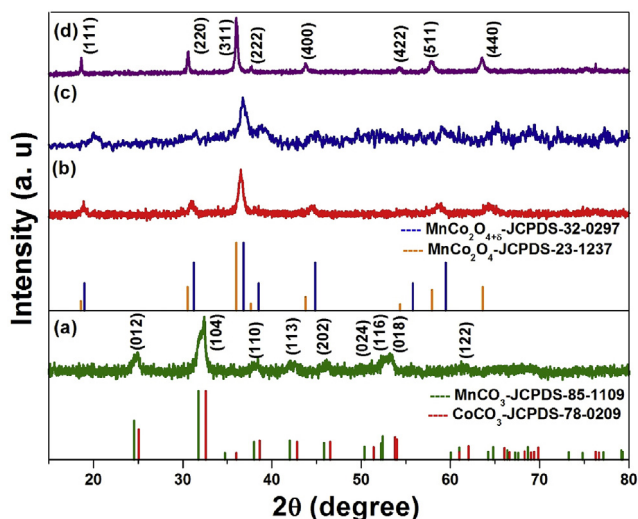
Fig. 1 — XRD pattern of as prepared MnCo₂O₄ (a), MnCo₂O₄ calcinated at 500 °C (b), N-MWCNT/MnCo₂O₄ calcinated at 500 °C (c), and MnCo₂O₄ calcinated at 800 °C for 3 h (d).

Fig. 2 — Raman spectra of M1, M2 and M3 samples (a—c).

Fig. 1(b, c) shows the XRD pattern of $MnCo_2O_4$ and N-doped MWCNT-$MnCo_2O_4$ calcinated at 500 °C. It indicates that the shifting of 2 theta values to higher angles that represents the excess oxygen present in the $MnCo_2O_4$ for the compound formation and the calculated d-spacing values are coinciding with the cubic system of non-stoichiometric $MnCo_2O_{4+\delta}$ phase (32-0297). The calculated lattice parameter values are, a = 8.1726 Å and cell volume (V) is 5.458 Å³ for $MnCo_2O_4$ (M1) and a = 7.962 Å, V = 5.0481 for N-doped MWCNT/$MnCo_2O_4$ (M2) samples. Further increasing the calcinations temperature to 800 °C (Fig. 1d), all diffraction peaks shifted to the lower angle (2θ) and are well matched with the cubic structure of $MnCo_2O_4$ phase with $Fd\overline{3}$ m space group (JCPDS no-23-1237) without any impurity phases and its lattice parameter value is a = 8.27 Å and V = 566.70 Å³, which is merely coincided with the standard data. The observed high intensity diffraction peaks elucidates the increase in crystallinity as well as grain size. The XRD results confirmed that while increasing the calcination temperature the excess oxygen is removed from the crystal structure of $MnCo_2O_{4+\delta}$ that leads to the formation of pure phase of $MnCo_2O_4$. The obtained results are well agreed with the previous reports [25].

Fig. 2(a—c) shows the Raman spectra of M1, M2 and M3 samples which indicate the Raman bands at three regions like 460—470 cm⁻¹, 600—610 cm⁻¹ and 660—670 cm⁻¹ corresponds to E_g, F_{2g} and A_{1g} modes of spinel $MnCo_2O_4$ [26]. The high wave number region (660—670 cm⁻¹) is assigned to the vibration of octahedral cations and F_{2g} and E_g mode gives the vibration of tetrahedral and octahedral sites respectively [27]. In the case of M2 sample, it consists of MWCNT which additionally shows the two bands at 1351 and 1599 cm⁻¹ that represents the sp³ hybridized disorder carbon (D-band) and sp² hybridized graphitic carbon (G-band) respectively [28].

The valence state of the prepared $MnCo_2O_4$ and N-doped MWCNT/$MnCo_2O_4$ is examined through XPS analysis and are given in Figs. 3 and 4. Fig. 3(a) shows the survey spectrum of
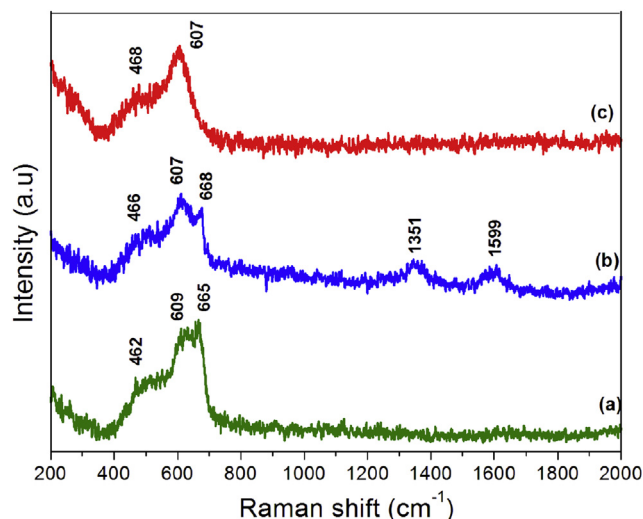
M3 sample that indicates the presents of Mn, Co, O and carbon from the substrate. Fig. 3(b) shows the two main peaks which is assigned to the Mn $2p_{1/2}$ and Mn $2p_{3/2}$ region and their deconvoluted spectra indicates the four broad peaks located at 642, 652.4, 643.4 and 654.8 eV. The 642 and 652.4 eV is corresponds to the binding energy of Mn^{2+} and 643.4 and 654.8 eV is related to the binding energy of Mn^{3+} valence state [29]. The deconvoluted spectra of Co 2p region Fig. 3(c) containing two sharp peaks and two satellite peaks. The two sharp peaks located at the binding energy of 781.9 and 796.1 eV corresponding to Co^{2+} and Co^{3+}, respectively. The observed two satellite peaks represents the cobalt exists in 2 + and 3 + valence state [30]. The oxygen 1s region shown in Fig. 3(d) which represents the two peaks at 529.8 and 531 eV corresponds to the metal-oxygen bonds in $MnCo_2O_4$ and metal-surface hydroxyl groups respectively [14,16]. The XPS result reveals that M3 sample consists of multivalence state of Mn and Co, including 2 + and 3 + valence state.

Fig. 4(a) represents survey spectrum of M2 sample, which indicates the presence of Mn, Co, O, C and N. Fig. 4(b and c) shows the deconvoluted spectra of Mn 2p and Co 2p region which implies that in $MnCo_2O_4$, Mn and Co element exist in mixed valence state as similar to M3 sample. Fig. 4(d) shows the deconvoluted spectra of O 2p region, it shows the five peaks at 529.8, 531, 531.8, 533.1 and 533.9 eV corresponds to binding energy of metal-oxygen bond, metal-hydroxyl groups, C—OH, O—C—O and —COOH functional groups respectively [31—33]. The deconvoluted spectra of carbon 1s region shown in Fig. 4(e), denotes the three peaks at 284.4, 285.1 and 286.6 eV, which are assigned to the C—C, C—O and C=O functional groups, respectively. In addition, Fig. 4(f) elucidate the presence of nitrogen content at 398.8 and 400.4 eV ascribed to the functional groups of pyridinic-N and pyrrolic-N and their atomic percentage are 1.77% and 1.65% respectively [34]. The XPS result elucidates that different functional groups and Mn and Co exist in multivalence state which confirms the composite consists of functionalized N-doped MWCNT/$MnCo_2O_4$ and clearly indicates that nitrogen content is
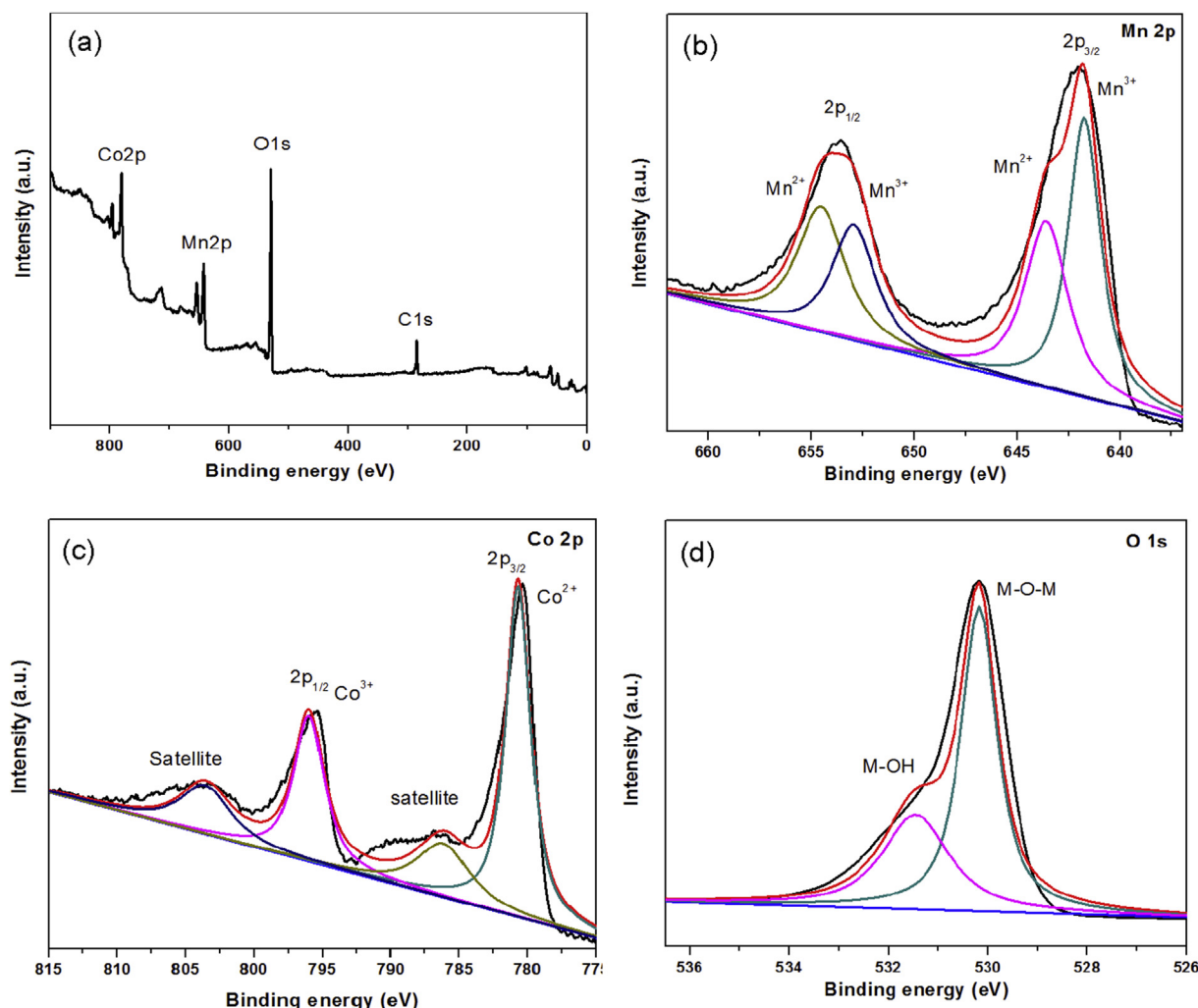
Fig. 3 – XPS survey spectrum of M3 sample (a) and deconvoluted spectra of Mn 2p (b), Co 2p (c), and O 1s (d).

attached to the MWCNT during hydrothermal treatment using ammonia as a starting precursor [34].

Fig. 5(a, b) represents the morphology of M1 sample which shows the formation of uniform microsphere in the size range between 6 and 9 μm. The formation and evaluation of $MnCo_2O_4$ is explained as follows. In the first step, metal acetates are dissolved into distilled water that produced its constituent metal and acetate ions. After that the aqueous ascorbic acid solution is added into the above solution there no obvious precipitation takes place. But, while adding ammonia, it produces more hydroxyl ions, which strongly interacts with metal ions to form a corresponding metal hydroxides precipitation. As well as this large amount of OH^- ions decrease the solution acidity and driven the nucleation as fast. Therefore, in a short while massive nanoparticles produced [35]. During the hydrothermal treatment, Ascorbic acid was oxidized into dehydro-ascorbic acid (DHA) and it is hydrolyzed into 2, 3-diketogulonic acid and again it oxidized to form the threonic acid and oxalate acid. Here, the threonic acid is produced the CO_3^- ions through deep oxidation process [36,37]. In high temperature around 200 °C, Metal hydroxides are converted into metal carbonates due to weak interaction between the hydroxyl group and metal ions through ion

exchange process [24]. Finally the $MnCO_3$ and $FeCO_3$ uniform microspheres were formed. Similarly, $MnCO_3$ is synthesized using L-lysine as a carbonate source that produced the CO_3^- ions after de-carboxylation process [38].

The evaluation of microsphere is mainly arises from two possible reactions. One is Ostwald ripening process where the big particles grown by the expense of smaller ones due to the process of dissolution and re-crystallization [39–43]. The next one is the self-aggregation mechanism where the nanoparticles have higher surface energy that minimizes the overall energy of the system; the nanoparticles underwent self-aggregation process [41,42]. In the present case, the generated $MnCO_3$ and $CoCO_3$ nanoparticles has high surface energy hence it minimizes the surface energy therefore the primary nanoparticles tend to aggregate each other and to form microsphere through self-assembly process. Here, there is no possible way for Ostwald ripening process because ammonia source has the ability to release the large amount of OH^- ions to the reactants, which induces the formation of large number of nanoparticles at the shorter time and simultaneously it prevent the dissolution and re-crystallization process [35,44]. In this self-assembly process, not only surface energy, crystal-face attraction, Van-der
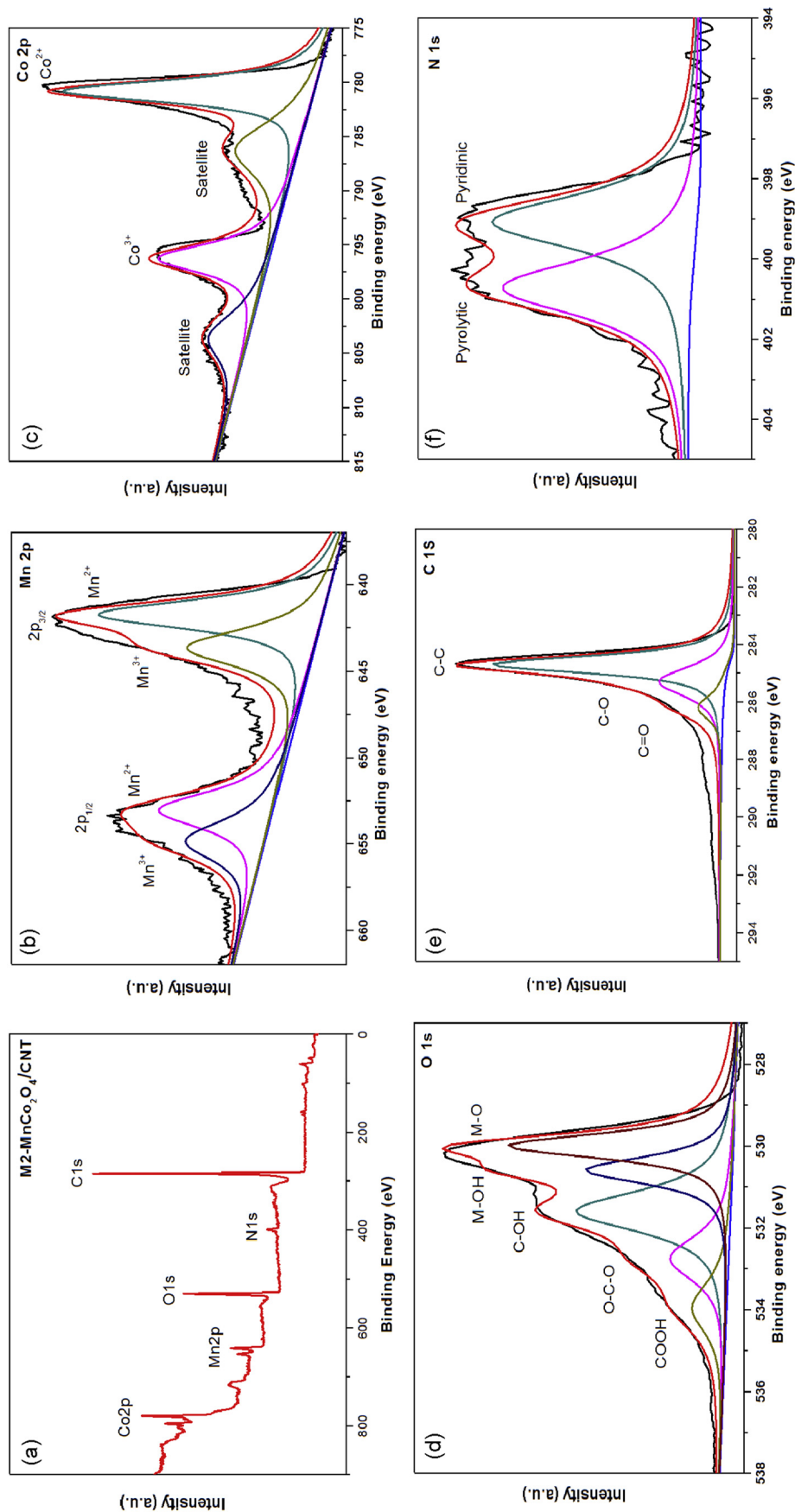
Fig. 4 — XPS survey spectrum of M2 sample (a), and deconvoluted spectra of Mn 2p (b), Co 2p (c), O 1s (d). C 1s (e) and N 1s (f).
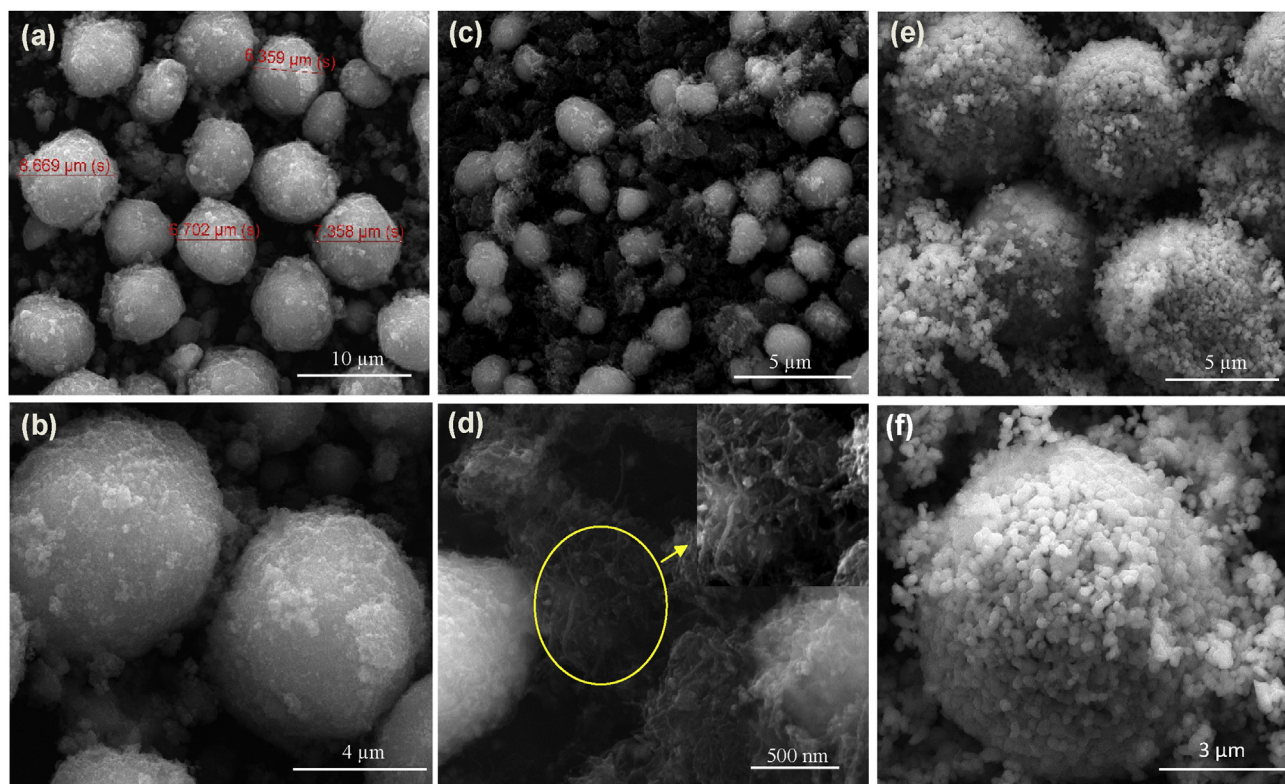
Fig. 5 — FESEM image of M1 (a, b), M2 (c, d), and M3 (e, f).

Waals forces and hydrogen bonds may also be involved [45,46]. Finally, the as-prepared sample is calcinated at 500 °C for 3 h, the metal carbonates are decomposed and leads to the formation of $MnCo_2O_4$ microsphere. The similar kind of observation is reported in elsewhere [24].

Fig. 5(c) shows the FESEM image of M2 sample. It can be seen that the N-doped MWCNT are uniformly distributed on the $MnCo_2O_4$ microspheres. Fig. 5(d) infers the interconnecting behaviour of N-doped MWCNT with $MnCo_2O_4$ and inset Fig. 5(d) clearly shows the coalescence of MWNCNT. The morphology of M3 sample is shown in Fig. 5(e, f), it shows the formation of microsphere which is obviously seen that individual nanoparticles and particle size exhibits in the range of 230 nm—250 nm. Compared M1 sample, the M3 sample has a larger particle size and enhance the crystallinity which causes due to heat treatment and it facilitates amorphous nanoparticles get agglomerate into larger particles that leads to alter the crystallinity of the sample [47].

The electrocatalytic ORR activity of M1, M2 and M3 catalysts was first evaluated using cyclic voltammetry. The cyclic voltammograms of electrodes were obtained by loading a thin film on glassy carbon electrode with active region of 0.1025 cm^2. The CVs show the onset potential value of 0.81, 0.83 and 0.86 V for M1, M2 and M3 electrodes, respectively (Fig. 6). The shift of ORR onset potential mainly comes from the incorporated structure of $MnCo_2O_4$ microsphere and nitrogen-doped MWCNT functionality.

Further, the kinetics of electrocatalytic oxygen reduction of N-doped $MWCNT/MnCo_2O_4$ was evaluated linear sweep voltammetry technique using rotating disk electrode (RDE) as working electrode experiments. A set of ORR linear sweep voltammogram traces from 400 to 2025 rpm in 0.1 M KOH solution at a scan rate 10 mVs^{-1} are presented in Fig. 7a. We have recorded ORR polarization data by linear sweep voltammetry technique (LSV) using rotating disk electrode as working electrode in order to access the kinetics of ORR for M1, M2 and M3 samples in O_2 saturated 0.1 M KOH electrolyte.
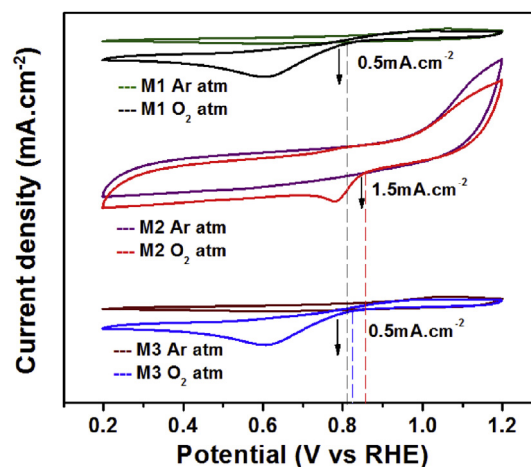

Fig. 6 — CV curves for M1, M2 and M3 in O_2 and Ar saturated 0.1 M KOH electrolyte at a scan rate of 10 mVs^{-1}. Catalyst loading: 0.25 mg cm^{-2}.

Fig. 8 – Chronoamperometric response of M2 and Pt/C on RDE electrode kept at 1600 rpm at applied potential of 0.70 V versus RHE in O_2-saturated 0.1 M KOH electrolyte.
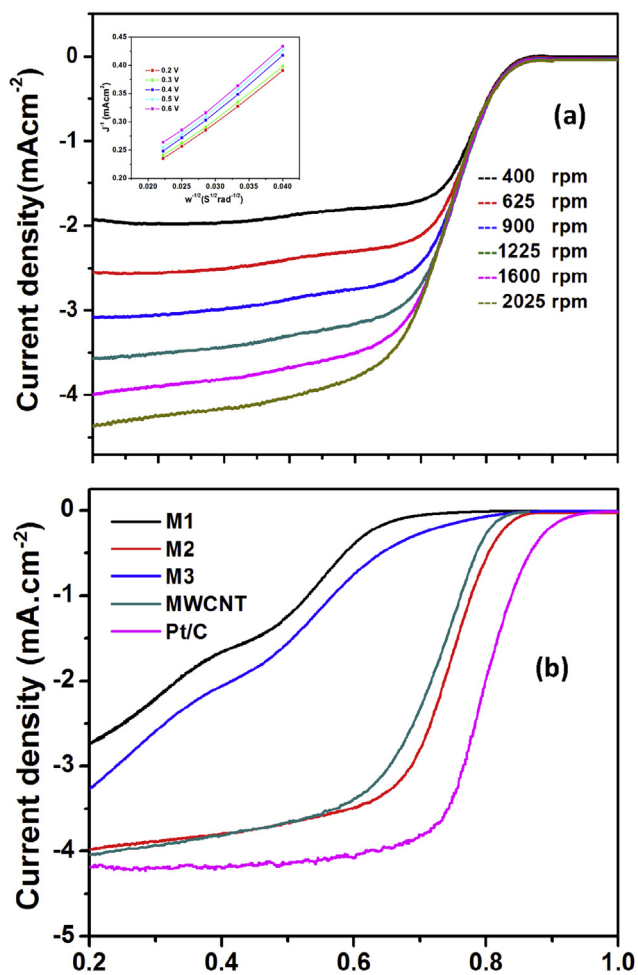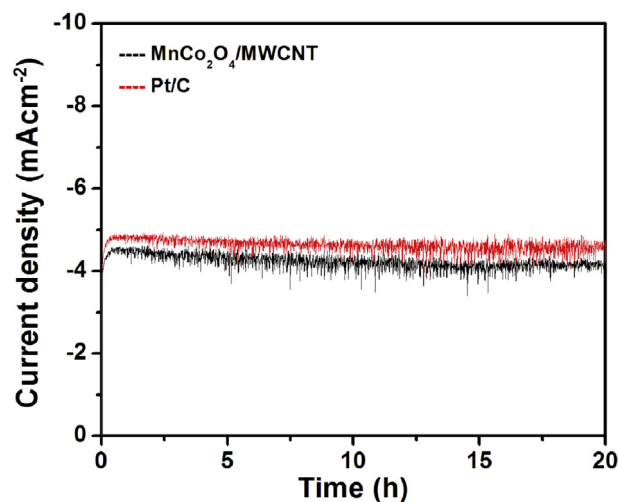
Fig. 7 – (a) Oxygen reduction reaction RDE curve for M2 in alkaline electrolyte at various rotation rates, (b) Comparison RDE plots for oxygen reduction reaction at 1600 rpm of M1, M2, M3 and Pt/C catalysts in 0.1 M KOH electrolyte at a scan rate of 10 mVs^{-1}. MWNCNT-MnCo$_2$O$_4$ loading on GCE is 0.25 mg cm^{-2}.

The polarization curve shows the diffusion limiting current and mixed kinetic diffusion control region, whereas the diffusion region limiting current starts from 0.7 V and ends with 0.86 V, and the mixed kinetic diffusion control region between 0.2 V and 0.7 V in case of M2 sample. The oxygen reduction half-wave potentials of M1, M2, M3 and MWCNT electrocatalysts were found to be 0.58, 0.75, 0.6 and 0.72 V, respectively. The $E_{1/2}$ of M2 is 30 mV higher than MWCNT electrocatalyst, 170 mV and 150 mV higher than M1 and M3 catalysts, respectively (Fig. 7b). Furthermore, MWNCNT-MnCo$_2$O$_4$ electrocatalyst showed a good diffusion-limited current suggesting better oxygen reduction activity compared with MnCo$_2$O$_4$ alone. This result significantly reveals that M2 has better electrocatalytic activity towards ORR than M1 and M3 samples evaluated at same amount of catalyst loading. Moreover, the oxygen reduction current observed for hybrid catalyst was 3 order of magnitude higher than M3, suggesting that the coupling effect of nitrogen functionality of MWCNT with MnCo$_2$O$_4$ microsphere. We compare the ORR activity of our catalyst with a commercial Pt/C catalyst (20 wt% on Vulcan carbon). The onset and half-wave potentials are about 0.92 and 0.81 V respectively, which are very close to M2 catalyst being 0.86 and 0.75 V, respectively. The varying rotation rate were used to derive a Kotchey–Levich plot (inset of Fig. 7a) with good linearity and slope remain constant over a wide potential range of 0.2–0.6 V, from which electron transfer number for oxygen reduction reaction on catalyst were calculated, with obtained value of 3.9 for M2- MWNCNT-MnCo$_2$O$_4$. This result suggests that ORR process catalyzed by our unique structured material proceed through highly favourable one step 4 electron transfer reaction. Further, we evaluated the long term stability of the M2 and Pt/C catalysts were assessed by chronoamperometry studies using RDE three electrode cell configurations at the applied potential of 0.7 V shown in Fig. 8. The resulting M2 catalytic stability last over 20 h, this performance comparably similar to commercial available Pt/C catalyst should be noted.

Conclusion

The N-doped MWCNT-MnCo$_2$O$_4$ microsphere was successfully prepared using a hydrothermal method. The phase purity, functional groups and oxidation state was thoroughly investigated through XRD, Raman and XPS analysis. The prepared MnCo$_2$O$_4$ exhibits the microsphere formation which is due to aggregation of smaller nanoparticles in an oriented attachment. The oxygen reduction half-wave potentials of MWNCNT-MnCo$_2$O$_4$ is 30 mV higher than MWCNT and 150 mV higher than MnCo$_2$O$_4$ catalyst. This enhanced electrocatalytic behaviour was attained through synergistic effect of MWCNT and MnCo$_2$O$_4$. Kotchey–Levich plot suggests that ORR process is occur through 4-electron transfer reaction. So this result assured that spinel type MnCo$_2$O$_4$ combined with MWNCNT is an efficient oxygen reduction reaction catalyst in alkaline electrolyte.

Acknowledgements

REFERENCES

[1] Spendelow JS, Wieckowski AA. Electrocatalysis of oxygen reduction and small alcohol oxidation in alkaline media. Phys Chem Chem Phys 2007;9:2654—75.

[2] Wang DH, Xin L, Hovden R, Wang H, Yu Y, Muller DA, et al. Structurally ordered intermetallic platinum—cobalt core—shell nanoparticles with enhanced activity and stability as oxygen reduction electrocatalysts. Nat Mater 2013;12:81—7.

[3] Wu ZS, Yang S, Sun Y, Parvez K, Feng X, Mullen K. 3D Nitrogen-doped graphene aerogel-supported Fe_3O_4 nanoparticles as efficient electrocatalysts for the oxygen reduction reaction. J Am Chem Soc 2012;134:9082—5.

[4] Sun M, Dong Y, Zhang G, Qu J, Li J. α-Fe_2O_3 spherical nanocrystals supported on CNTs as efficient non-noble electrocatalysts for the oxygen reduction reaction. J Mater Chem A 2014;2:13635—40.

[5] Zhang H, Liu X, He G, Zhang X, Bao S, Hu W. Bioinspired synthesis of nitrogen/sulfur co-doped graphene as an efficient electrocatalyst for oxygen reduction reaction. J Power Sources 2015;279:252—8.

[6] Wang W, Wang R, Ji S, Feng H, Wang H, Lei Z. Pt overgrowth on carbon supported PdFe seeds in the preparation of core—shell electrocatalysts for the oxygen reduction reaction. J Power Sources 2010;195:3498—503.

[7] Winter M, Brodd RJ. What are batteries, fuel cells and supercapacitors? Chem Rev 2004;104:4245—70.

[8] Selvakumar K, Senthil Kumar SM, Thangamuthu R, Kruthika G, Murugan P. Development of shape-engineered α-MnO_2 materials as bi-functional catalysts for oxygen evolution reaction and oxygen reduction reaction in alkaline medium. Int J Hydrogen Energy 2014;39:21024—36.

[9] Xu J, Gao P, Zhao TS. Non-precious Co_3O_4 nano-rod electrocatalyst for oxygen reduction reaction in anion-exchange membrane fuel cells. Energy Environ Sci 2012;5:5333—9.

[10] Bikkarolla S, Yu F, Zhou W, Joseph P, Cumpson P, Papakonstantinou PA. Three dimensional Mn_3O_4 network supported on a nitrogenated graphene electrocatalyst for efficient oxygen reduction reaction in alkaline media. J Mater Chem A 2014;2:14493—501.

[11] Rios E, Reyes H, Ortiz J, Gautier JL. Double channel electrode flow cell application to the study of HO_2^- production on $Mn_xCo_{3-x}O_4$ ($0 \le x \le 1$) spinel films. Electrochim Acta 2005;50:2705—11.

[12] Cheng F, Shen J, Peng B, Pan Y, Tao Z, Chen J. Rapid room-temperature synthesis of nanocrystalline spinels as oxygen reduction and evolution electrocatalysts. Nat Chem 2011;3:79—84.

[13] Liang Y, Wang H, Zhou J, Li Y, Wang J, Regier T, et al. Covalent hybrid of spinel manganese—cobalt oxide and graphene as advanced oxygen reduction electrocatalysts. J Am Chem Soc 2012;134:3517—23.

[14] Ge X, Liu Y, Thomas Goh FW, Andy Hor TS, Zong Y, Xiao P, et al. Dual-phase spinel $MnCo_2O_4$ and spinel $MnCo_2O_4$/ nanocarbon hybrids for electrocatalytic oxygen reduction and evolution. ACS Appl Mater Interfaces 2014;6:12684—91.

[15] Du J, Pan Y, Zhang T, Han X, Cheng F, Chen J. Facile solvothermal synthesis of $CaMn_2O_4$ nanorods for electrochemical oxygen reduction. J Mater Chem 2012;22:15812—8.

[16] Hamdani M, Singh RN, Chartier P. Co_3O_4 and Co- based spinel oxides bifunctional oxygen electrodes. Int J Electrochem Sci 2010;5:556—7.

[17] Prabu M, Ketpang K, Shanmugam S. Hierarchical nanostructured $NiCo_2O_4$ as an efficient bifunctional non-precious metal catalyst for rechargeable zinc—air batteries. Nanoscale 2014;6:3173—318.

[18] Wang J, Xin H, Zhu J, Liu S, Wu Z, Wang D. 3D hollow structured Co_2FeO_4/MWCNT as an efficient non-precious metal electrocatalyst for oxygen reduction reaction. J Mater Chem A 2015;3:1601—8.

[19] Eder D. Carbon nanotube-inorganic hybrids. Chem Rev 2010;110:1348—85.

[20] Deng DH, Yu L, Chen XQ, Wang GX, Jin L, Pan XL, et al. Iron Encapsulated within Pod-like carbon nanotubes for oxygen reduction reaction. Angew Chem Int Ed 2013;52:371—5.

[21] Yang Z, Zhou X, Nie H, Yao Z, Huang S. Facile construction of manganese oxide doped carbon nanotube catalysts with high activity for oxygen reduction reaction and investigations into the origin of their activity enhancement. ACS Appl Mater Interfaces 2011;3:2601—6.

[22] Ciric-Marjanovic G, Pasti I, Mentus S. One-dimensional nitrogen-containing carbon nanostructures. Prog Mater Sci 2015;69:61—182.

[23] Li J, Xiong S, Li X, Qian Y. A facile route to synthesize multiporous $MnCo_2O_4$ and $CoMn_2O_4$ spinel quasi-hollow spheres with improved lithium storage properties. Nanoscale 2013;5:2045—54.

[24] Xiong QQ, Tu JP, Shi SJ, Liu XY, Wang XL, Gu CD. Ascorbic acid-assisted synthesis of cobalt ferrite ($CoFe_2O_4$) hierarchical flower-like microspheres with enhanced lithium storage properties. J Power Sources 2014;256:153—9.

[25] Nissinen T, Leskela M, Gasik M, Lamminen J. Decomposition of mixed Mn and Co nitrates supported on carbon. Thermochim Acta 2005;427:155—61.

[26] Zhang Y, Liu S, Li Y, Deng D, Si X, Ding Y, et al. Electrospun graphene decorated $MnCo_2O_4$ composite nanofibers for glucose biosensing. Biosens Bioelectron 2015;66:308—15.

[27] Bahlawane N, Ngamou PHT, Vannier V, Kottke T, Heberle J, Hoinghaus KK. Tailoring the properties and the reactivity of the spinel cobalt oxide. Phys Chem Chem Phys 2009;11:9224—32.

[28] Amiri A, Shanbedi M, Eshghi H, Heris SZ, Baniadam M. Highly dispersed multiwalled carbon nanotubes decorated with Ag nanoparticles in water and experimental investigation of the thermophysical properties. J Phys Chem C 2012;116:3369—75.

[29] Fu C, Li G, Luo D, Huang X, Zheng J, Li L. One-step calcination-free synthesis of multicomponent spinel assembled microspheres for high-performance anodes of Li-ion batteries: a case study of $MnCo_2O_4$. ACS Appl Mater Interfaces 2014;6:2439—49.

[30] Yuvaraj S, Amaresh S, Lee YS, Kalai Selvan R. Effect of carbon coating on the electrochemical properties of Co_2SnO_4 for negative electrodes in Li-ion batteries. RSC Adv 2014;4:6407—16.

[31] Liu J, Qian D, Feng H, Li J, Jiang J, Peng S, et al. Designed synthesis of TiO_2-modified iron oxides on/among carbon nanotubes as a superior lithium-ion storage material. J Mater Chem 2014;2:11372—81.

[32] Luo Y, Luo J, Jiang J, Zhou W, Yang H, Qi X, et al. Seed-assisted synthesis of highly ordered TiO_2@α-Fe_2O_3 core/shell arrays

on carbon textiles for lithium-ion battery applications. Energy Environ Sci 2012;5:6559–66.

[33] Pradhan GK, Parida KM. Fabrication, growth mechanism, and characterization of α-Fe$_2$O$_3$ nanorods. ACS Appl Mater Interfaces 2011;3:317–23.

[34] Wang L, Yin F, Yao C. N-doped graphene as a bifunctional electrocatalyst for oxygen reduction and oxygen evolution reactions in an alkaline electrolyte. J Hydrogen Energy 2014;39:15913–9.

[35] Zhao Z, Miyuchi M. Shape modulation of tungsten oxide hollow structures. J Phys Chem C 2009;113:6539.

[36] Rojas AM, Gerschenson LN. Ascorpic acid destruction in aqueous model systems: an additional discussion. J Sci Food Agric 2001;81:1433–9.

[37] Tang WT, Li SD, Chen Y. In: Energy and Environmental Engineering-Wu, editor. Controlled synthesis of manganese oxides with different morphologies and their performance for catalytic removal of gaseous benzene. London: Taylor and Francis Group; 2015, ISBN 978-1-138-02665-0. p. 47–51.

[38] Zhou L, Kong X, Gao M, Lian F, Li B, Zhou Z, et al. Hydrothermal fabrication of MnCO$_3$@rGO composite as an anode material for high-performance lithium ion batteries. Inorg Chem 2014;53:9228–34.

[39] Xu L, Shen J, Lu C, Chen Y, Hou W. Self-assembled three-dimensional architectures of Y$_2$(WO$_4$)$_3$:Eu: controlled synthesis, growth mechanism, and shape-dependent luminescence properties. Cryst Growth Des 2009;9:3129–36.

[40] He Z, Chen Z, Li Y, Zhang Q, Wang H. Molar ratio of in to urea directed formation of In$_2$O$_3$ hierarchical structures: cubes and nanorod-flowers. CrystEngComm 2011;13:2557–65.

[41] Xu L, Lu C, Zhang Z, Yang X, Hou W. Various self-assembled three-dimensional hierarchical architectures of La$_2$(MoO$_4$)$_3$: controlled synthesis, growth mechanisms, luminescence properties and adsorption activities. Nanoscale 2010;2:995–1005.

[42] Yuvaraj S, Karthikeyan K, Kalai Selvan R. Surfactant free hydrothermal synthesis of hierarchical structured spherical CuBi$_2$O$_4$ as negative electrodes for Li-ion hybrid capacitors. J Colloidal Interfaces 2016;469:47–56.

[43] Penn RL, Oskam G, Strathmann TJ, Searson PC, Stone AT, Veblan DR. Epitaxial assembly in aged colloids. J Phys Chem B 2001;105:2177–82.

[44] Zhao ZG, Miyauchi M. Shape modulation of tungstic acid and tungsten oxide hollow structures. J Phys Chem C 2009;113:6539–46.

[45] Hu L, Qu B, Li C, Chen Y, Mei L, Lei D, et al. Facile synthesis of uniform mesoporous ZnCo$_2$O$_4$ microspheres as a high-performance anode material for Li-ion batteries. J Mater Chem A 2013;1:5596–602.

[46] Colfen H, Antonietti M. Mesocrystals: inorganic superstructures made by highly parallel crystallization and controlled alignment. Angew Chem Int Ed 2005;44:5576–91.

[47] Frandsen C, Legg BA, Comolli LR, Zhang H, Gilbert B, Johnson E, et al. Aggregation-induced growth and transformation of β-FeOOH nanorods to micron- sized α-Fe$_2$O$_3$ spindles. CrystEngComm 2014;16:1451–8.